How to cite: *Angew. Chem. Int. Ed.* **2024**, *63*, e202320027
doi.org/10.1002/anie.202320027

Electrocatalytic NO_3^- Reduction

Modulating the Electronic Structure of Cobalt in Molecular Catalysts via Coordination Environment Regulation for Highly Efficient Heterogeneous Nitrate Reduction

*Libo Sun, Chencheng Dai, Tianjiao Wang, Xindie Jin, Zhichuan J. Xu, and Xin Wang**

Abstract: Ammonia (NH_3) is pivotal in modern industry and represents a promising next-generation carbon-free energy carrier. Electrocatalytic nitrate reduction reaction (eNO_3RR) presents viable solutions for NH_3 production and removal of ambient nitrate pollutants. However, the development of eNO_3RR is hindered by lacking the efficient electrocatalysts. To address this challenge, we synthesized a series of macrocyclic molecular catalysts for the heterogeneous eNO_3RR. These materials possess different coordination environments around metal centers by surrounding subunits. Consequently, electronic structures of the active centers can be altered, enabling tunable activity towards eNO_3RR. Our investigation reveals that metal center with an N_2(pyrrole)-N_2(pyridine) configuration demonstrates superior activity over the others and achieves a high NH_3 Faradaic efficiency (FE) of over 90 % within the tested range, where the highest FE of approximately 94 % is obtained. Furthermore, it achieves a production rate of 11.28 $mg\,mg_{cat}^{-1}\,h^{-1}$, and a turnover frequency of up to 3.28 s^{-1}. Further tests disclose that these molecular catalysts with diverse coordination environments showed different magnetic moments. Theoretical calculation results indicate that variated coordination environments can result in a d-band center variation which eventually affects rate-determining step energy and calculated magnetic moments, thus establishing a correlation between electronic structure, experimental activity, and computational parameters.

Introduction

Ammonia (NH_3) holds immense significance as a vital industrial chemical worldwide for the production of fertilizers, pharmaceutical products, explosives, etc.[1] It is also regarded as an ideal energy carrier with no carbon emission due to its high energy density and hydrogen capacity.[2] However, traditional NH_3 synthesis methods, such as the highly energy-intensive Haber–Bosch process, contribute significantly to carbon emission,[3] necessitating alternative approaches for NH_3 production. Direct NH_3 synthesis from electrocatalytic N_2 fixation under mild conditions has garnered considerable interest. Nevertheless, it suffers from a poor reaction rate,[4] primarily due to the high dissociation energy required to break the triple N≡N bond (941 $kJ\,mol^{-1}$).[5] Conversely, nitrate, as an environmental pollutant,[6] features a significantly lower dissociation energy for N=O bond (204 $kJ\,mol^{-1}$).[7] This characteristic ensures more facile reaction kinetics for NH_3 synthesis through electrocatalytic nitrate reduction (eNO_3RR) than N_2 reduction. Therefore, employing nitrate as the reactant offers not only an easier pathway for NH_3 production but also a means for simultaneous nitrate removal.

However, the complexity of the eNO_3RR process, which involves a multi-step electron and hydrogen transfer process and the formation of various products such as nitrite, nitric oxide, nitrous oxide, and dinitrogen, etc., poses a challenge to the development of efficient and selective catalysts.[8] Towards that end, molecular catalysts have emerged as promising candidates for facilitating the conversion of nitrate to NH_3. Their advantage lies in their well-defined structures, and the ability to control reaction pathways by precisely designing the active centers.[9] The activity of molecular catalysts can be tuned through several factors,[10] such as the metal center, the coordinating ligands surrounding the metal center,[11] the oxidation state of the metal,[12] and external stimuli like magnetic fields,[13] etc. Therefore, the atomic-level construction of molecular electrocatalysts with desired configurations is instrumental in deciphering the reaction mechanism, enhancing comprehension of

[*] Dr. L. Sun, Prof. X. Wang
Department of Chemistry, City University of Hong Kong, Kowloon, 999077, Hong Kong SAR, P. R. China
E-mail: wang.xin@cityu.edu.hk

Dr. L. Sun, Dr. C. Dai, T. Wang, X. Jin, Prof. Z. J. Xu
Cambridge Centre for Advanced Research and Education in Singapore Ltd (Cambridge CARES), CREATE Tower, Singapore 138602, Singapore

Dr. C. Dai, Prof. Z. J. Xu
School of Material Science and Engineering, Nanyang Technological University, 50 Nanyang Avenue, Singapore, 639798 Singapore

Prof. X. Wang
Hong Kong Branch of National Precious Metals Material Engineering Research Center, City University of Hong Kong, Kowloon, 999077, Hong Kong SAR, P. R. China

structure–activity relationships, and providing guidance for the design of promising electrocatalysts for practical applications.[14]

Conventional macrocyclic molecular catalysts, such as metal in porphyrin and phthalocyanine, are coordinated by four nitrogen atoms from surrounding pyrrole subunits.[15] These macrocyclic structures have demonstrated promising catalytic performance in a range of electrocatalytic reactions, including CO_2 reduction, oxygen reduction, nitrate reduction, etc.[13e,16] Extensive efforts have been devoted to unraveling the influence of diverse coordination environments on the catalytic activity of active sites in these reactions through various model systems.[17] For instance, in the context of single-atom catalysts, metal active sites coordinated with a higher proportion of nitrogen from the pyridine component have exhibited enhanced performance compared to other types of nitrogen in other reactions.[18] However, this conclusion is shadowed by the complex nature of the single-atom catalysts as they are normally prepared by pyrolysis, which imposes challenges in the structure characterization of such materials.[8j] To tackle this limitation, we developed macrocyclic molecular catalysts with precise composition and explored the difference between pyridine and pyrrole subunits in electrocatalytic CO_2 reduction.[19] Our findings reveal that active centers coordinated with pyridine subunits consistently exhibit significantly improved activity compared to pyrrole ones for CO_2 reduction. This result has sparked our interest in further exploring the electrocatalytic behaviors of metal centers coordinated with different types of ligands and their impact on the activity for eNO_3RR.

In our previous study,[19] we recognized that the comparison of different types of active sites based on different structure models, such as cobalt 7,10-Di(quinolin-8-yl)Pyrazino[2,3-*f*][1,10]Phenanthroline (CoQPyPhen), 5,10,15,20-Tetraphenyl-21H,23H-porphine cobalt (CoPor), cobalt phthalocyanine (CoPC) casted some shadow on the investigation, due to possible differences brought in by the use of different structure models. To better address this issue and more accurately evaluate the activity of diverse coordinating active centers, it is preferable to prepare and compare different active sites based on a single type of structure model. In this study, we focus on modifying the coordination environment to construct a series of macrocyclic cobalt complexes based on the 1,10-phenanthroline configuration employed in our previous research.[19] By introducing different configurations surrounding the metal center (Figure 1a), including N_4(pyridine) in cobalt 7,10-Di(quinolin-8-yl)Pyrazino[2,3-*f*][1,10]Phenanthroline (CoQPyPhen), N_2(pyridine)-N_2(pyrrole) in cobalt (3^2Z,3^3Z)-4-phenyl-1^1H,3^2H-2(7,10)-pyrazino[2,3-*f*][1,10]phenanthrolina-1,3(7,2)-diindolacyclobutaphane (CoQPyPhenI), and N_2-(pyridine)-O_2(phenol) in cobalt 2,2′-(pyrazino[2,3-*f*]-[1,10]phenanthroline-7,10-diyl)diphenol (CoQPyPhenO), we effectively tune the electronic structures of cobalt complexes. Among these configurations, the cobalt complex based on N_2(pyridine)-N_2(pyrrole) exhibits significantly higher activity and selectivity compared to the others. It demonstrates a substantially lower overpotential for

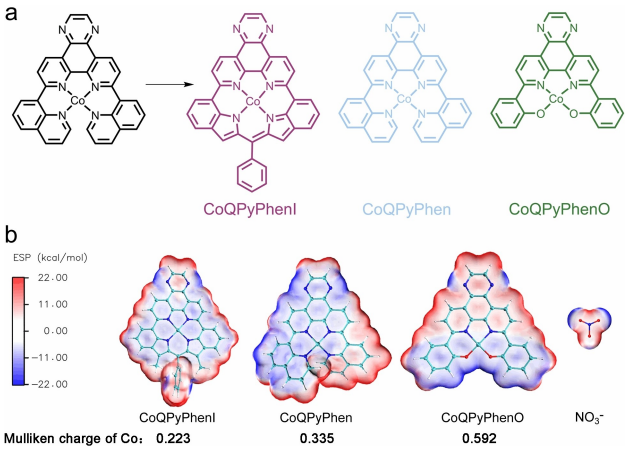

Figure 1. a) Illustration of CoQPyPhenI, CoQPyPhen, and CoQPyPhenO used. b) Calculated ESP figures and Mulliken charge of cobalt elements in CoQPyPhenI, CoQPyPhen, and CoQPyPhenO.

eNO_3RR to NH_3, achieving an impressive NH_3 Faradaic efficiency (FE) exceeding 90% across the entire test potential range. Subsequent analysis reveals differences in the magnetic moment of these complexes, where the magnetic moment is correlated to experimental turnover frequency. Moreover, computational analysis reveals a correlation between the magnetic moment, the d-band center, and the potential of the rate-determining step. These findings establish a relationship between the electronic structure, catalytic activity, and computational parameters, guiding to enhance eNO_3RR activity towards NH_3 synthesis.

Results and Discussion

We applied the design of the 1,10-phenanthroline core from our previous research to assemble three types of active centers with different electronic structures:[19] CoQPyPhen with N_4(pyridine), CoQPyPhenI with N_2(pyridine)-N_2-(pyrrole), CoQPyPhenO with N_2(pyridine)-O_2(phenol) configuration, as depicted in Figure 1a. Computational methods were first employed to investigate the electronic structure differences of these molecular structures. The electronegativity difference of nitrogen and oxygen elements can induce charge polarization,[20] and the nitrogen elements from pyrrole of the indole and pyridine of the 1,10-phenanthroline can contribute to slight differences in valence state.[19] As the electronegativity of nitrogen and oxygen is different, the use of pyridine and pyrrole subunits also brings in diverse coordination abilities. These factors combined can allow the tuning of the electronic structure of the active cobalt centers. Indeed, the electrostatic potential (ESP) calculations in Figure 1b present different electrostatic potential surfaces, which may result in diverse electronic structures surrounding active centers. A further Mulliken charge calculation suggested that the cobalt elements obey an oxidation state of CoQPyPhenI < CoQPyPhen < CoQPyPhenO. The above results suggested from a computational perspective that these molecule models designed based on

the 1,10-phenanthroline core indeed exhibit diverse electronic structures, which may result in different catalytic activities.

The metal valence states of the metal complexes were then investigated using X-ray photoelectron spectroscopy (XPS). To better understand the oxidation state of cobalt elements in these materials, the oxidation state of CoPC was compared as a reference in the XPS measurements. As shown in Figure 2a, the cobalt oxidation states of the three metal complexes follow a trend of CoQPyPhenI < CoQPyPhen < CoQPyPhenO based on the peak shift of Co $3d_{3/2}$. Further analysis by X-ray absorption near edge structure (XANES) measurements was also conducted for Co K-edge of these materials (Figure 2b), which also suggested the same trend of cobalt valence states of catalysts. The near-edge line of CoQPyPhenO is closer to that of Co_3O_4, which indicates its higher valence state, meanwhile, the valence state of CoQPyPhenI is the lowest. These results suggest that the electronic structures surrounding the cobalt active centers altered by diverse coordination moieties can change the valence state of the cobalt element.[10b]

These metal complexes were immobilized onto multi-walled carbon nanotubes (CNT) to obtain heterogeneous molecular electrocatalysts (CoQPyPhenO/CNT, CoQPyPhen/CNT, and CoQPyPhenI/CNT). The immobilization process resulted in a change of the I_D/I_G ratio observed in the Raman spectra tests, as shown in Figure 2c. This I_D/I_G ratio change can be attributed to different loading amounts of these metal complexes. Besides, the successful immobilization onto CNT can also lead to a disruption of the local environment of the carbon substrate, leading to the change of I_D/I_G ratio.[21] High-resolution transmission electron microscopy (HR-TEM) image and high-angle annular dark-field scanning transmission electron microscopy (HAADF-STEM) image of CoQPyPhenI/CNT, depicted in Figure 2d–2e, confirm CoQPyPhenI successfully loaded onto CNT uniformly without the formation of nanoparticles. Furthermore, the integrity of the CNT structure remains intact, ensuring its conductivity for subsequent electrocatalytic processes. Energy dispersive X-ray spectroscopy (EDS-mapping) images (Figure 2f) demonstrated the uniform dispersion of CoQPyPhenI onto CNT.

To assess the electrocatalytic activity of these metal complexes for eNO_3RR, these samples were drop-casted onto carbon strips and tested in a three-electrode H-cell with an electrolyte composed of 0.1 mol K_2SO_4 and 0.1 mol KNO_3. Linear sweep voltammetry (LSV) tests were first conducted to compare the eNO_3RR activity of these metal complexes with different coordination subunits. As shown in Figure 3a, CoQPyPhenI/CNT exhibits the highest activity and CoQPyPhen demonstrates the lowest activity among these three complexes. The much lower current density from the bare CNT confirms that the active sites primarily originate from the metal complex rather than the bare CNT. The notable activity disparity prompted further evaluation of product selectivity through potentiostatic tests, where the generated NH_3 products were quantified with ultraviolet-visible (UV/Vis) spectrophotometry (details provided in the experimental section and Figure S3).

The potentiostatic test results depicted in Figure 3b–3d agree with the LSV results. Specifically, at an initial potential of around −0.40 V vs. RHE (reversible hydrogen electrode) with an average partial current density of 3.73 mA cm^{-2}, NH_3 product was detected with a FE of approximately 56.53 %, corresponding to an NH_3 yield rate of 0.288 mg mg_{cat}^{-1} h^{-1} based on the loading of CoQPyPhenI/CNT (Table S1). The NH_3 FE increased to approximately 90.75 % at −0.45 V vs. RHE and reached a maximum of ca.

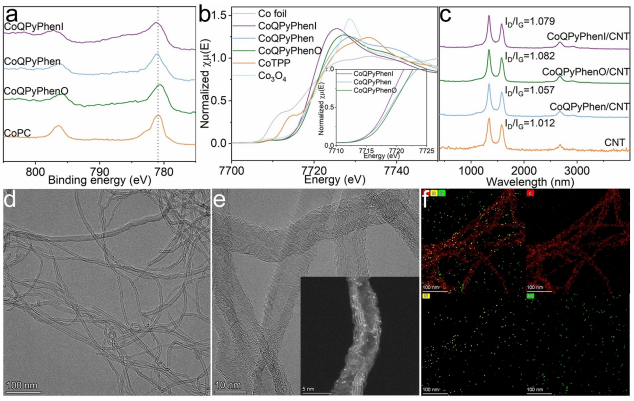

Figure 2. a) Co $3d_{3/2}$ and $3d_{1/2}$ X-ray photoelectron spectra. b) Co K-edge XANES data. c) Raman spectra after immobilization. d–e) Transmission electron microscopy images of CoQPyPhenI/CNT, inset: high-angle annular dark-field scanning transmission electron microscopy image of CoQPyPhenI/CNT. f) EDS-mapping images of CoQPyPhenI/CNT.

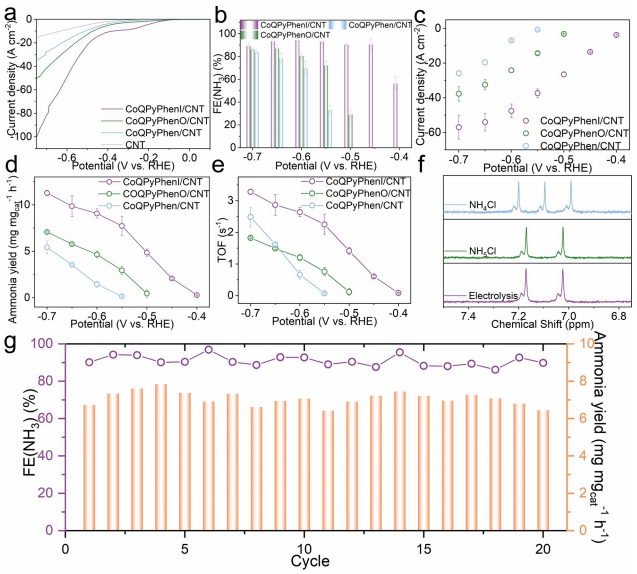

Figure 3. a) Polarization curves of CoQPyPhenI/CNT, CoQPyPhenO/CNT, CoQPyPhen/CNT and bare CNT. b) Comparison of Faradaic efficiency of CoQPyPhenI/CNT, CoQPyPhenO/CNT, and CoQPyPhen/CNT. c). The partial current densities during electrocatalytic nitrate reduction. d) Ammonia yield calculated. e) Turnover frequency calculated. f) ^1H NMR data comparison with isotope nitrate. g) Durability test of CoQPyPhenI/CNT at −0.5 V vs. RHE. Each cycle lasts 1 hr.

94.29 % at −0.6 V vs. RHE, with a partial current density of ca. 47.51 mA cm^{-2}, and an NH_3 production rate of 9.075 mg mg_{cat}^{-1} h^{-1}. For comparison, other kinds of electrocatalysts, such as Fe single-atom catalysts reported in K_2SO_4/KNO_3 electrolyte achieved a NH_3 FE of ca. 39 % at −0.50 V vs. RHE with a current density of 4.30 mA cm^{-2}.[8j] They reach the maximum FE of ca. 75 % at −0.65 V vs. RHE with a partial current density of 35.30 mA cm^{-2}, and yield 5.245 mg mg_{cat}^{-1} h^{-1}. The turnover frequency (TOF) is also given in Figure 3e, where a TOF of 3.28 s^{-1} was reached at −0.70 V vs. RHE.

To validate the results obtained from UV/Vis tests and exclude the influence of possible NH_3 contamination from sources other than nitrate, isotopic labeling experiments were performed using ^{1}H nuclear magnetic resonance (^{1}H NMR) tests. Since the concentration of NH_3 product generated from nitrate reduction was sufficiently high, ^{1}H NMR tests could be conducted. As depicted in Figure 3f, triple peaks are observed at around 7.12, 7.02, and 6.91 ppm when $^{14}NH_4^+$ is used to label the position, which is consistent with the peaks obtained with $^{14}NO_3^-$ as the reactant. Furthermore, double peaks appear at a chemical shift of 7.09 and ca. 6.94 ppm when $^{15}NH_4^+$ is used, corresponding to the peaks obtained when $^{15}NO_3^-$ is the reactant. This observation confirms the consistency of the results obtained using both isotopic labeling and UV/Vis tests and also excludes potential contamination from external sources.

The durability of CoQPyPhenI/CNT in eNO_3RR to ammonia was then assessed through 20 consecutive electrolysis cycles in the H-cell at −0.50 V vs. RHE (Figure 3g). Although the FE and NH_3 yield rate fluctuated slightly, the average FE remained above 90 % and NH_3 yield consistently ranged between 6 to 8 mg mg_{cat}^{-1} h^{-1}. XPS tests were conducted on the sample before and after durability tests. Although the signal quality becomes poorer, the cobalt peak is still detectable, indicating the good stability of CoQPyPhenI/CNT throughout the testing period.

Furthermore, in order to understand the electronic structure of these metal complexes, their effective magnetic moments were evaluated and normalized to the cobalt element, as shown in Figure 4a. Notably, CoQPyPhenI exhibits the highest effective magnetic moment. The experimental activity of these materials is also found to correlate with their magnetic behaviours. As illustrated in Figure 4b, the TOF selected at −0.55 V vs. RHE increases with the increasing normalized magnetic moment at 300 K. This finding hints that the regulation of electronic structure is effective in fine-tuning the activity of electrocatalysts for eNO_3RR.

To demonstrate the advantage of CoQPyPhenI over commercial molecular catalysts, CoPor and CoPC were immobilized onto CNT and tested for eNO_3RR. As illustrated in Figure 4c, CoPC/CNT and CoPor/CNT reach an NH_3 FE of only 80.49 % and 67.90 %, respectively, at approximately −0.65 V vs. RHE. These results further emphasize the superior performance of CoQPyPhenI as a promising molecular catalyst for eNO_3RR. In addition, the advantage of utilizing piperidine in 1,10-phenanthroline functional group-derived molecular catalysts has been previously demonstrated in electrocatalytic CO_2 reactions as well. To examine whether this is still valid for eNO_3RR, two other molecular catalysts cobalt (4^1*E*,4^2*Z*)-5-phenyl-1^1*H*,4^2*H*-1,4(7,2)-diindola-2,3(2,6)-dipyridinacyclopentaphane (CoQPyBPYI) and cobalt (3^2*Z*,3^3*Z*)-4-phenyl-1^1*H*,3^2*H*-2(3,6)-dipyrido[3,2-*a*:2′,3′-*c*]phenazina-1,3(7,2)-diindolacyclobutaphane (CoBPhNQPyPhenI) derived without a piperidine or with a quinoxaline group were synthesized (Figure S5 and S6). When employed in eNO_3RR, CoQPyBPYI/CNT exhibits significantly worse activity, with the highest NH_3 FE of only 77 % (Figure S5). The NH_3 FE on CoBPhNQPyPhenI is also inferior to CoQPyPhenI (Figure S6). These comparisons highlight the importance of employing both piperidine and 1,10-phenanthroline functional groups other than solely N_2(pyridine)-N_2(pyrrole) moiety for the eNO_3RR molecular catalyst synthesis.

The loading effect of CoQPyPhenI in eNO_3RR was also investigated by drop-casting the electrocatalyst onto a carbon strip with different loadings (1.63 μg cm^{-2}, 3.26 μg cm^{-2}, and 6.52 μg cm^{-2} based on cobalt element). From Figure S7, it was observed that the FE slightly increases with an increasing amount of CoQPyPhenI. To mitigate any potential mass transport influence, all the data reported are based on the loading of 1.63 μg cm^{-2}.

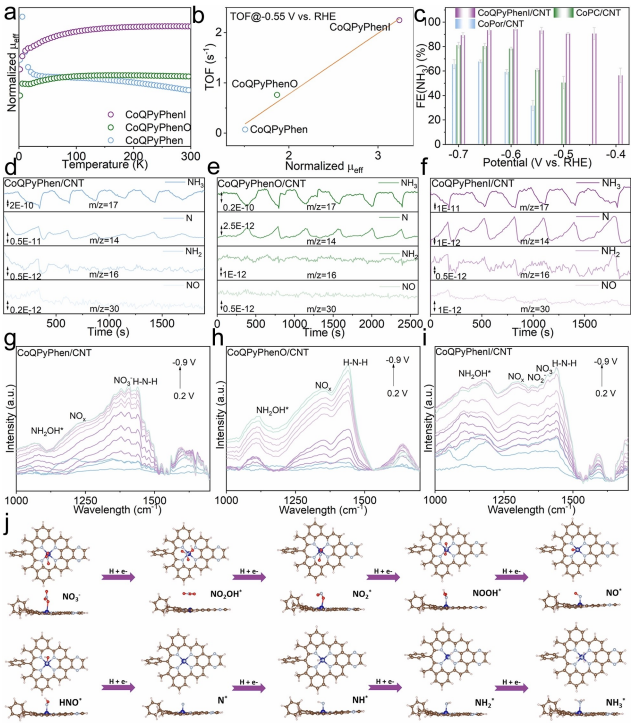

Figure 4. a) Normalized effective magnetic moments. b) The relationship between normalized magnetic effective moment and turnover frequency. c) Comparison of Faradaic efficiency of CoQPyPhenI/CNT, CoPC/CNT, and CoPor/CNT. Online mass data of CoQPyPhen/CNT (d), CoQPyPhenO/CNT (e), and CoQPyPhenI/CNT (f) during the reaction. In situ ATR-FTIR spectra of CoQPyPhen (g), CoQPyPhenO (h), and CoQPyPhenI (i) during the reaction. j) Illustration of reaction path on CoQPyPhenI.

Moreover, the molecular intermediates and products during eNO_3RR were detected by online mass spectrometry,[22] as shown in Figure 4d–4f. During a manually controlled 6 cycles of 120 or 240 s potentiostatic test at −0.55 V vs. RHE, the m/z signals of 14, 16, 17, 30 that correspond to N, NH_2, NH_3, and NO, can be observed for CoQPyPhenI/CNT (Figure 4f). For comparison, obvious signals belonging to only N and NH_3 can be found for other catalysts, which indicates a different binding strength towards certain intermediates. Subsequently, the in situ attenuated total reflectance-Fourier transform infrared spectroscopy (ATR-FTIR) measurements were performed in the range of 0.2 to −0.9 V vs. RHE to identify the adsorbates.[14a,23] As illustrated in Figure 4g–4i, the adsorption bands at around 1392 and 1358 cm^{-1} are ascribed to the N–O symmetric and asymmetric stretching vibration of NO_3^-. Another peak observed at around 1110 cm^{-1} is ascribed to the –N–O– stretching vibration of the key NH_2OH* intermediate during eNO_3RR. The characteristic peak at around 1450 cm^{-1} represents the H–N–H vibration. The stronger N–O vibration observed for CoQPyPhenI/CNT suggests stronger adsorption towards NO_3^- for such a material than the others. A possible reaction pathway is hence proposed based on the above results, which are given in Figure 4j and referenced in the computational section.

The density functional theory (DFT) calculations were then conducted to investigate the reaction mechanism of nitrate reduction on these metal complexes. The calculated Gibbs free energy change, along with the related intermediates and reaction pathway, are shown in Figure 5a–5c. The initial step involves the adsorption of NO_3^- onto the substrate, forming the NO_3* intermediate, which spontaneously accepts a proton from the solution to form the NO_2OH* intermediate without electron transfer. The subsequent reaction of NO_2OH* intermediate proceeds through eight proton-coupled electron transfer steps, leading to the formation of various intermediates (NO_2*–NOOH*–NO*–HNO*–N*–NH*–NH_2*–NH_3*) before the final release of NH_3 (Figure 4j). The results show that the release of NH_3 requires a slightly higher potential compared to other steps in the reaction pathway, making it the rate-determining step (RDS) for CoQPyPhen and CoQPyPhenO. On the other hand, the adsorption of NO_3^- demands higher energy for CoQPyPhenI.

Partial density of states (PDOS) analysis of cobalt d orbitals reveals that these models exhibit semi-metal state properties with electron densities crossing the Fermi levels (Figure 5d–5f). However, the different electron densities crossing the Fermi levels suggest variations in their conducting abilities, with CoQPyPhenI exhibiting the highest conductivity. The main contribution at that position originates from the dz2 orbital of cobalt, as indicated in Figure 5f. Considering that the formation of NO_3* is the RDS for CoQPyPhenI and the binding strength of NH_3* is critical for a timely release of the product, the electronic structures of CoQPyPhenI with the formation of key intermediates of NO_3* and NH_3* was given in Figure 5g–5h. From PDOS, a relatively larger resonance of the dz2-pz and dxz-px orbitals is observed with the formation of NO_3*, where a relatively lower resonance of dz2-pz is found for the formation of NH_3*, indicating a stronger binding of the former one than the latter one with the surface of CoQPyPhenI. Bader charges analysis (inset Figure 5g–5h) of CoQPyPhenI with NO_3* and NH_3* indicates intuitively that there is almost no bond formation between cobalt and NH_3*, resulting in significant charge depletion (blue color). In contrast, charge accumulation (yellow color) is observed between cobalt and NO_3*. This suggests a significant difference in the electronic structure of CoQPyPhenI with the presence of NO_3* and NH_3*. Our experimental results have already shown that, due to different coordination environments, the active centers of these electrocatalysts exhibit different magnetic moments, which shows a positive correlation with the activity (TOF) of these electrocatalysts. To understand from the computational perspective (Figure 5i), the d-band center (ε), magnetic moment, and rate-determining step (RDS) energy of these models were computed. The RDS energy is found to decrease with increasing d band center and the magnetic moment, which is in agreement with the experimental observation that TOF increases with the magnetic moment. Therefore, a relationship between the computed parameters, the measured normalized effective magnetic moment, and the experimental activity can be established. This provides valuable insights into the electronic structure–activity-computational parameter correlation, facilitating the understanding of the mechanism and future development of electrocatalysts.

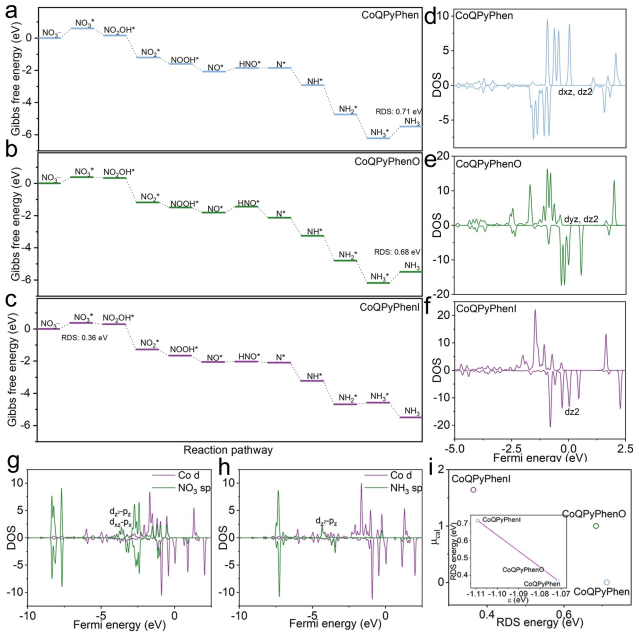

Figure 5. a–c) Gibbs free energy diagrams on CoQPyPhen, CoQPyPhenO, and CoQPyPhenI. d–f) The projected density of states (PDOS) of Co d orbitals for CoQPyPhen, CoQPyPhenO, and CoQPyPhenI. g–h) Charge density difference and PDOS analyses of CoQPyPhenI with NO_3* and NH_3*. i) The d-band center (ε) versus rate-determining step energy, and rate-determining step energy versusmagnetic moment.

Conclusion

In conclusion, electrocatalytic nitrate reduction holds great promise for NH_3 production and the remediation of nitrate from contaminated water sources. In this study, we employed cobalt-based molecular catalysts that were modified by coordinating surrounding subunits. Our analysis reveals that different coordination environments can induce diverse electronic structures, resulting in varying activity towards eNO_3RR. Among the cobalt complexes investigated, CoQ-PyPhenI prepared with an N_2(pyridine)-N_2(pyrrole) core, exhibits significantly enhanced activity and selectivity towards NH_3 production than the others. By conducting magnetic moment tests, a correlation between the experimental turnover frequency and the effective magnetic moments can be established, thus explaining experimentally the closed relationship between activity and electronic structure. Furthermore, it is found that the computational parameters, such as the rate-determining step energy could be correlated with the calculated magnetic moments and d band center, which demonstrates computationally the influence of electronic structures on the reaction activity. This sheds light on the impact of coordinating subunits on the electronic structures and activity towards eNO_3RR based on our system. These findings contribute to an insightful understanding of the mechanism and guide the future design of promising electrocatalysts for efficient eNO_3RR to NH_3.

Supporting Information

The authors have cited additional references within the Supporting Information.

Acknowledgements

This project was supported by the National Research Foundation (NRF), Prime Minister's Office, Singapore, under its Campus for Research Excellence and Technological Enterprise (CREATE) program. X.W. acknowledges the startup grant by the City University of Hong Kong (Grant No. 9020005), ITF-RTH—Global STEM Professorship (9446008), and Hong Kong Branch of National Precious Metals Material Engineering Research Center—ITC Fund.

Conflict of Interest

The authors declare no conflict of interest.

Data Availability Statement

The data that support the findings of this study are available from the corresponding author upon reasonable request.

Keywords: electrocatalysis · heterogeneous molecular catalysts · molecular catalysts · electrocatalytic nitrate reduction · macrocyclic

[1] H. Wan, A. Bagger, J. Rossmeisl, *Angew. Chem.* **2021**, *133*, 22137–22143.
[2] a) S. Mukherjee, S. V. Devaguptapu, A. Sviripa, C. R. F. Lund, G. Wu, *Appl. Catal. B* **2018**, *226*, 162–181; b) N. M. Adli, H. Zhang, S. Mukherjee, G. Wu, *J. Electrochem. Soc.* **2018**, *165*, J3130.
[3] H. Liu, *Chin. J. Catal.* **2014**, *35*, 1619–1640.
[4] a) G. Soloveichik, *Nat. Catal.* **2019**, *2*, 377–380; b) X. Fu, J. B. Pedersen, Y. Zhou, M. Saccoccio, S. Li, R. Sažinas, K. Li, S. Z. Andersen, A. Xu, N. H. Deissler, *Science* **2023**, *379*, 707–712.
[5] M. Falcone, L. Barluzzi, J. Andrez, F. Fadaei Tirani, I. Zivkovic, A. Fabrizio, C. Corminboeuf, K. Severin, M. Mazzanti, *Nat. Chem.* **2019**, *11*, 154–160.
[6] Y. Wang, Y. Yu, R. Jia, C. Zhang, B. Zhang, *Natl. Sci. Rev.* **2019**, *6*, 730–738.
[7] A. Stirling, I. Pápai, J. Mink, D. R. Salahub, *J. Chem. Phys.* **1994**, *100*, 2910–2923.
[8] a) S. Han, H. Li, T. Li, F. Chen, R. Yang, Y. Yu, B. Zhang, *Nat. Catal.* **2023**, *6*, 402–414; b) R. Jia, Y. Wang, C. Wang, Y. Ling, Y. Yu, B. Zhang, *ACS Catal.* **2020**, *10*, 3533–3540; c) Y. Wang, W. Zhou, R. Jia, Y. Yu, B. Zhang, *Angew. Chem. Int. Ed.* **2020**, *59*, 5350–5354; d) J. Wang, C. Cai, Y. Wang, X. Yang, D. Wu, Y. Zhu, M. Li, M. Gu, M. Shao, *ACS Catal.* **2021**, *11*, 15135–15140; e) W. He, J. Zhang, S. Dieckhöfer, S. Varhade, A. C. Brix, A. Lielpetere, S. Seisel, J. R. C. Junqueira, W. Schuhmann, *Nat. Commun.* **2022**, *13*, 1129; f) Y. Kong, L. Wu, X. Yang, Y. Li, S. Zheng, B. Yang, Z. Li, Q. Zhang, S. Zhou, L. Lei, G. Wu, Y. Hou, *Adv. Funct. Mater.* **2022**, *32*, 2205409; g) Y. Kong, Y. Li, X. Sang, B. Yang, Z. Li, S. Zheng, Q. Zhang, S. Yao, X. Yang, L. Lei, *Adv. Mater.* **2022**, *34*, 2103548; h) L. Han, X. Liu, J. Chen, R. Lin, H. Liu, F. Lü, S. Bak, Z. Liang, S. Zhao, E. Stavitski, J. Luo, R. R. Adzic, H. L. Xin, *Angew. Chem. Int. Ed.* **2019**, *58*, 2321–2325; i) H. Liu, X. Lang, C. Zhu, J. Timoshenko, M. Rüscher, L. Bai, N. Guijarro, H. Yin, Y. Peng, J. Li, *Angew. Chem. Int. Ed.* **2022**, *61*, e202202556; j) Z.-Y. Wu, M. Karamad, X. Yong, Q. Huang, D. A. Cullen, P. Zhu, C. Xia, Q. Xiao, M. Shakouri, F.-Y. Chen, J. Y. Kim, Y. Xia, K. Heck, Y. Hu, M. S. Wong, Q. Li, I. Gates, S. Siahrostami, H. Wang, *Nat. Commun.* **2021**, *12*, 2870; k) J. Li, M. Li, N. An, S. Zhang, Q. Song, Y. Yang, J. Li, X. Liu, *Proc. Natl. Acad. Sci. USA* **2022**, *119*, e2123450119; l) M. Karamad, T. J. Goncalves, S. Jimenez-Villegas, I. D. Gates, S. Siahrostami, *Faraday Discuss.* **2023**, *243*, 502–519.
[9] a) L. Sun, V. Reddu, A. C. Fisher, X. Wang, *Energy Environ. Sci.* **2020**, *13*, 374–403; b) S.-L. Meng, C. Zhang, C. Ye, J.-H. Li, S. Zhou, L. Zhu, X.-B. Li, C.-H. Tung, L.-Z. Wu, *Energy Environ. Sci.* **2023**, *16*, 1590–1596; c) G.-F. Chen, Y. Yuan, H. Jiang, S.-Y. Ren, L.-X. Ding, L. Ma, T. Wu, J. Lu, H. Wang, *Nat. Energy* **2020**, *5*, 605–613.
[10] a) M. A. Halcrow, *Dalton Trans.* **2020**, *49*, 15560–15567; b) B.-H. Lee, H. Shin, A. S. Rasouli, H. Choubisa, P. Ou, R. Dorakhan, I. Grigioni, G. Lee, E. Shirzadi, R. K. Miao, J. Wicks, S. Park, H. S. Lee, J. Zhang, Y. Chen, Z. Chen, D. Sinton, T. Hyeon, Y.-E. Sung, E. H. Sargent, *Nat. Catal.* **2023**, *6*, 234–243.
[11] L. Sun, Z. Huang, V. Reddu, T. Su, A. C. Fisher, X. Wang, *Angew. Chem. Int. Ed.* **2020**, *59*, 17104–17109.
[12] P. Cao, X. Quan, X. Nie, K. Zhao, Y. Liu, S. Chen, H. Yu, J. G. Chen, *Nat. Commun.* **2023**, *14*, 172.
[13] a) Z. Sun, L. Lin, J. He, D. Ding, T. Wang, J. Li, M. Li, Y. Liu, Y. Li, M. Yuan, B. Huang, H. Li, G. Sun, *J. Am. Chem. Soc.* **2022**, *144*, 8204–8213; b) A. Cao, V. J. Bukas, V. Shadravan, Z.

Wang, H. Li, J. Kibsgaard, I. Chorkendorff, J. K. Nørskov, *Nat. Commun.* **2022**, *13*, 2382; c) W. J. Sun, H. Q. Ji, L. X. Li, H. Y. Zhang, Z. K. Wang, J. H. He, J. M. Lu, *Angew. Chem. Int. Ed.* **2021**, *60*, 22933–22939; d) N. Chebotareva, T. Nyokong, *J. Appl. Electrochem.* **1997**, *27*, 975–981; e) F. Lv, M. Sun, Y. Hu, J. Xu, W. Huang, N. Han, B. Huang, Y. Li, *Energy Environ. Sci.* **2023**, *16*, 201–209; f) Z. Jiang, Y. Wang, Z. Lin, Y. Yuan, X. Zhang, Y. Tang, H. Wang, H. Li, C. Jin, Y. Liang, *Energy Environ. Sci.* **2023**, *16*, 2239–2246; g) C. He, Z.-Y. Wu, L. Zhao, M. Ming, Y. Zhang, Y. Yi, J.-S. Hu, *ACS Catal.* **2019**, *9*, 7311–7317.

[14] a) J.-Y. Fang, Q.-Z. Zheng, Y.-Y. Lou, K.-M. Zhao, S.-N. Hu, G. Li, O. Akdim, X.-Y. Huang, S.-G. Sun, *Nat. Commun.* **2022**, *13*, 7899; b) Z. Xu, L. Wan, Y. Liao, M. Pang, Q. Xu, P. Wang, B. Wang, *Nat. Commun.* **2023**, *14*, 1619.

[15] E. Boutin, L. Merakeb, B. Ma, B. Boudy, M. Wang, J. Bonin, E. Anxolabéhère-Mallart, M. Robert, *Chem. Soc. Rev.* **2020**, *49*, 5772–5809.

[16] a) S. Fukuzumi, Y.-M. Lee, H. S. Ahn, W. Nam, *Chem. Sci.* **2018**, *9*, 6017–6034; b) S. Dey, B. Mondal, S. Chatterjee, A. Rana, S. Amanullah, A. Dey, *Nat. Chem. Rev.* **2017**, *1*, 0098; c) E. Boutin, M. Robert, *Trends Chem.* **2021**, *3*, 359–372; d) S. Lyu, C. Guo, J. Wang, Z. Li, B. Yang, L. Lei, L. Wang, J. Xiao, T. Zhang, Y. Hou, *Nat. Commun.* **2022**, *13*, 6171.

[17] J. Wang, S. Dou, X. Wang, *Sci. Adv.* **2021**, *7*, eabf3989.

[18] X. Cui, S. Yang, X. Yan, J. Leng, S. Shuang, P. M. Ajayan, Z. Zhang, *Adv. Funct. Mater.* **2016**, *26*, 5708–5717.

[19] L. Sun, V. Reddu, S. Xi, C. Dai, Y. Sheng, T. Su, A. C. Fisher, X. Wang, *Adv. Energy Mater.* **2022**, *12*, 2202108.

[20] L. Zhang, Y. Jia, H. Liu, L. Zhuang, X. Yan, C. Lang, X. Wang, D. Yang, K. Huang, S. Feng, X. Yao, *Angew. Chem. Int. Ed.* **2019**, *58*, 9404–9408.

[21] a) D. Ma, S. Han, S. Zhou, W. Wei, X. Li, B. Chen, X. Wu, Q. Zhu, *CCS Chemistry* **2023**, *5*, 1827–1840; b) J. Su, C. B. Musgrave III, Y. Song, L. Huang, Y. Liu, G. Li, Y. Xin, P. Xiong, M. M.-J. Li, H. Wu, M. Zhu, H. Chen, J. Zhang, H. Shen, B. Tang, M. Robert, W. A. Goddard III, R. Ye, *Nat. Catal.* **2023**, *6*, 818–828.

[22] C. Guo, W. Zhou, X. Lan, Y. Wang, T. Li, S. Han, Y. Yu, B. Zhang, *J. Am. Chem. Soc.* **2022**, *144*, 16006–16011.

[23] a) K. Fan, W. Xie, J. Li, Y. Sun, P. Xu, Y. Tang, Z. Li, M. Shao, *Nat. Commun.* **2022**, *13*, 7958; b) S. Han, H. Li, T. Li, F. Chen, R. Yang, Y. Yu, B. Zhang, *Nat. Catal.* **2023**, *6*, 402–414.

Manuscript received: December 27, 2023
Accepted manuscript online: February 6, 2024
Version of record online: February 21, 2024